

A common-path interferometer for time-resolved and shot-noise-limited detection of single nanoparticles

Meindert A. van Dijk, Markus Lippitz*, Daniël Stolwijk,
and Michel Orrit

MoNOS, Huygens Laboratory, Universiteit Leiden, P.O. Box 9504, 2300 RA Leiden, The Netherlands

* present address: 4. Physical Institute, University of Stuttgart, and Max Planck Institute for Solid State Research, Heisenbergstrasse 1, 70569 Stuttgart, Germany

orrit@molphys.leidenuniv.nl

<http://www.monos.leidenuniv.nl/>

Abstract: We give a detailed description of a novel method for time-resolved experiments on single non-luminescent nanoparticles. The method is based on the combination of pump-probe spectroscopy and a common-path interferometer. In our interferometer, probe and reference arms are separated in time and polarization by a birefringent crystal. The interferometer, fully described by an analytical model, allows us to separately detect the real and imaginary contributions to the signal. We demonstrate the possibilities of the setup by time-resolved detection of single gold nanoparticles as small as 10 nm in diameter, and of acoustic oscillations of particles larger than 40 nm in diameter.

© 2007 Optical Society of America

OCIS codes: (120.3180) Interferometry; (180.0180) Microscopy; (300.6500) Spectroscopy, time-resolved

References and links

1. Special issue on Single Molecules, *Science* **283**(5408), 1593–1804 (1999).
2. M. A. van Dijk, M. Lippitz, and M. Orrit, "Far-field optical microscopy of single metal nanoparticles," *Accounts Chem. Res.* **38**, 594–601 (2005).
3. M. A. van Dijk, A. L. Tchegbotareva, M. Orrit, M. Lippitz, S. Berciaud, D. Lasne, L. Cognet, and B. Lounis, "Absorption and scattering microscopy of single metal nanoparticles," *Phys. Chem. Chem. Phys.* **8**, 3486–3495 (2006).
4. L. Cognet, C. Tardin, D. Boyer, D. Choquet, P. Tamarat, and B. Lounis, "Single metallic nanoparticle imaging for protein detection in cells," *Proc. Natl. Acad. Sci. U. S. A.* **100**, 11350–11355 (2003).
5. M. A. van Dijk, M. Lippitz, and M. Orrit, "Detection of acoustic oscillations of single gold nanospheres by time-resolved interferometry," *Phys. Rev. Lett.* **95**, 267406 (2005).
6. R. C. Jin, J. E. Jureller, H. Y. Kim, and N. F. Scherer, "Correlating second harmonic optical responses of single Ag nanoparticles with morphology," *J. Am. Chem. Soc.* **127**, 12482–12483 (2005).
7. S. Berciaud, L. Cognet, P. Tamarat, and B. Lounis, "Observation of intrinsic size effects in the optical response of individual gold nanoparticles," *Nano Lett.* **5**, 515–518 (2005).
8. O. L. Muskens, N. Del Fatti, and F. Vallée, "Femtosecond response of a single metal nanoparticle," *Nano Lett.* **6**, 552–556 (2006).
9. M. Lippitz, M. A. van Dijk, and M. Orrit, "Third-harmonic generation from single gold nanoparticles," *Nano Lett.* **5**, 799–802 (2005).
10. P. Stoller, V. Jacobsen, and V. Sandoghdar, "Measurement of the complex dielectric constant of a single gold nanoparticle," *Opt. Lett.* **31**, 2474–2476 (2006).

11. A. Arbouet, D. Christofilos, N. Del Fatti, F. Vallée, J. R. Huntzinger, L. Arnaud, P. Billaud, and M. Broyer, "Direct measurement of the single-metal-cluster optical absorption," *Phys. Rev. Lett.* **93**, 127401 (2004).
12. K. Lindfors, T. Kalkbrenner, P. Stoller, and V. Sandoghdar, "Detection and spectroscopy of gold nanoparticles using supercontinuum white light confocal microscopy," *Phys. Rev. Lett.* **93**, 037401 (2004).
13. F. V. Ignatovich and L. Novotny, "Real-time and background-free detection of nanoscale particles," *Phys. Rev. Lett.* **96**, 013901 (2006).
14. D. Boyer, P. Tamarat, A. Maali, B. Lounis, and M. Orrit, "Photothermal imaging of nanometer-sized metal particles among scatterers," *Science* **297**, 1160–1163 (2002).
15. S. Berciaud, L. Cognet, G. A. Blab, and B. Lounis, "Photothermal heterodyne imaging of individual nonfluorescent nanoclusters and nanocrystals," *Phys. Rev. Lett.* **93**, 257402 (2004).
16. R. H. J. Kop and R. Sprik, "Phase-sensitive interferometry with ultrashort optical pulses," *Rev. Sci. Instrum.* **66**, 5459–5463 (1995).
17. F. Zernike, "Phase contrast, a new method for the microscopic observation of transparent objects," *Physica* **9**, Part I, 686–698, Part II, 974–986 (1942).
18. J. Hwang, M. M. Fejer, and W. E. Moerner, "Scanning interferometric microscopy for the detection of ultrasmall phase shifts in condensed matter," *Phys. Rev. A* **73**, 021802 (2006).
19. M. J. LaGasse, D. Liu-Wong, J. G. Fujimoto, and H. A. Haus, "Ultrafast switching with a single-fiber interferometer," *Opt. Lett.* **14**, 311–313 (1989).
20. N. S. Patel, K. L. Hall, and K. A. Rauschenbach, "Interferometric all-optical switches for ultrafast signal processing," *Appl. Opt.* **37**, 2831–2842 (1998).
21. D. H. Hurley and O. B. Wright, "Detection of ultrafast phenomena by use of a modified Sagnac interferometer," *Opt. Lett.* **24**, 1305–1307 (1999).
22. Y. Sugawara, O. B. Wright, O. Matsuda, M. Takigahira, Y. Tanaka, S. Tamura, and V. E. Gusev, "Watching ripples on crystals," *Phys. Rev. Lett.* **88**, 185504 (2002).
23. T. Tachizaki, T. Muroya, O. Matsuda, Y. Sugawara, D. H. Hurley, and O. B. Wright, "Scanning ultrafast Sagnac interferometry for imaging two-dimensional surface wave propagation," *Rev. Sci. Instrum.* **77**, 043713 (2006).
24. F. L. Pedrotti and L. S. Pedrotti, *Introduction to Optics* (Prentice Hall, 1993).
25. H.-A. Bachor, *A Guide to Experiments in Quantum Optics* (Wiley-VCH, 1998).
26. R. J. McIntyre, "Multiplication Noise In Uniform Avalanche Diodes," *IEEE Trans. Electron Devices* **ED13**, 164–168 (1966).
27. U. Kreibig and M. Vollmer, *Optical Properties of Metal Clusters*, vol. 25 of *Springer Series in Materials Science* (Springer, Berlin, 1995).
28. M. Perner, S. Gresillon, J. Marz, G. von Plessen, J. Feldmann, J. Porstendorfer, K. J. Berg, and G. Berg, "Observation of hot-electron pressure in the vibration dynamics of metalnanoparticles," *Phys. Rev. Lett.* **85**, 792–795 (2000).
29. M. Perner, P. Bost, U. Lemmer, G. von Plessen, J. Feldmann, U. Becker, M. Mennig, M. Schmitt, and H. Schmidt, "Optically induced damping of the surface plasmon resonance in gold colloids," *Phys. Rev. Lett.* **78**, 2192–2195 (1997).
30. G. V. Hartland, "Measurements of the material properties of metal nanoparticles by time-resolved spectroscopy," *Phys. Chem. Chem. Phys.* **6**, 5263–5274 (2004).
31. N. Del Fatti, C. Voisin, F. Chevy, F. Vallée, and C. Flytzanis, "Coherent acoustic mode oscillation and damping in silver nanoparticles," *J. Chem. Phys.* **110**, 11484–11487 (1999).
32. H. Lamb, "On the Vibrations of an Elastic Sphere," *Proceedings of the London Mathematical Society* **13**, 189–212 (1882).
33. J. H. Hodak, A. Henglein, and G. V. Hartland, "Size dependent properties of Au particles: Coherent excitation and dephasing of acoustic vibrational modes," *J. Chem. Phys.* **111**, 8613–8621 (1999).
34. C. Voisin, D. Christofilos, P. A. Loukakos, N. Del Fatti, F. Vallée, J. Lerme, M. Gaudry, E. Cottancin, M. Pellarin, and M. Broyer, "Ultrafast electron-electron scattering and energy exchanges in noble-metal nanoparticles," *Phys. Rev. B* **69**, 195416 (2004).

1. Introduction

For the last 15 years, single-molecule spectroscopy has mainly focused on luminescence studies of fluorescent molecules and semiconductor nanocrystals [1]. In the last few years, however, ever increasing interest in the properties and applications of metal nanoparticles (nanospheres, nanorods, etc., with sizes between 1 and 100 nm) has stimulated the development of various optical detection schemes for single metal nanoparticles. Two recent articles have reviewed the general far-field optical methods for the detection of single nanoparticles [2], and more particularly the absorption and scattering-based methods [3]. An attractive characteristic of gold nanoparticles is their high photostability. Unlike dyes or semiconductor nanocrystals, gold par-

ticles do not suffer from photobleaching or photoblinking, which makes them appealing labels for biophysicists [4]. Another strong motivation is the study of original physical properties of metal nanoparticles, that often differ from those of the bulk metal, and to a large extent can be tuned through the size and shape of the nanoparticle. This sensitivity to size and shape, however, makes studies of ensembles of nanoparticles particularly vulnerable to distributions in sizes, shapes, crystal defects, etc.. Isolating a single particle once and for all eliminates inhomogeneous broadening and any implicit averaging inherent to even the most carefully selected ensembles. Only single-particle experiments permit to study a particle's elastic interaction with its specific close environment [5], to correlate optical and structural properties [6], or to obtain new insight in their linear and nonlinear optical properties [7, 8, 9].

The number of available methods for the detection of single metal nanoparticles has grown rapidly in the last few years [2]. Of all these methods, interferometric detection of the scattered field seems very promising, mainly because the interferometric signal drops as the third power of the particle size only, whereas the direct scattering signal drops as the sixth power, but also for the possibility to detect the full complex response of a nanoparticle [5, 10]. In all interferometric experiments, the field scattered by a single metal nanoparticle is mixed with a reference field, but the methods differ in their choices for the reference and scattered field [3]. Using the incident wave itself as a reference, one basically measures absorption [11]. Alternatively, the reference wave can be the reflection from the substrate on which the particle has been deposited [12], or an external reflection in a Michelson interferometer [13]. The signal wave can be either directly scattered by the particle, or indirectly scattered from a local inhomogeneity of refractive index, for example induced by heat released by the excited particle into its surroundings, as done in the photothermal method [14, 15]. In a recent work, we have used a common-path interferometer to measure the time-resolved response of single gold nanoparticles down to a 10-nm diameter [5]. This sensitive technique allowed us to detect acoustic vibrations of single gold nanoparticles. The present paper presents a more detailed description of our interferometer and its full characterization.

In our common-path interferometer, probe and reference arms are spatially overlapped (in contrast to, for example, Michelson and Mach-Zehnder interferometers [16]). The interfering waves are distinguished on the basis of both polarization and time, although any single one of these characteristics would in principle suffice. Temporal separations can be created via a relative delay between laser pulses, as done here, or via a small phase shift between two CW beams, as for example in phase-contrast microscopy [17], or by counter propagation in a Sagnac ring interferometer, as was recently implemented by Hwang et al. [18], for the phase-sensitive detection of very weak absorbers. The first implementation of a common-path interferometer in combination with pulsed laser sources was published by LaGasse et al. [19] in an optical switching experiment. In this experiment, the probe pulse was delayed by means of polarizing beam splitters and mirrors. Patel et al. [20] have built a number of logical elements by using the same technique, but with a birefringent fiber as a delay medium. Hurley and Wright [21] constructed a common-path interferometer based on a Sagnac interferometer, also using diversion through polarizing beam splitters to split a pulse into probe and reference. Polarization analysis allowed them to separately detect pump-induced changes in reflectivity and phase. Using this method, the same group were able to image the progression of pump-induced acoustic waves along a surface [22, 23].

We also rely on a polarization-induced delay between a probe pulse and a reference pulse, but we use a birefringent crystal as beamsplitter. The main advantage of this element is its simplicity and ease of alignment, which leads to a high contrast of the interference pattern. The delay between the interfering wavetrains in combination with a pump-probe configuration allows us to obtain information on ultrafast properties of the nanoparticles, and the high sensi-

tivity and low noise floor enables experiments on single nanoparticles. By choosing the proper configuration for the polarization optics of our interferometer, we can separate the detection of amplitude and phase changes induced by a single nanoparticle on the probe pulse, and measure the full complex response of the particle. Although we used our interferometer only for gold nanoparticles so far, the method is in principle applicable to any absorbing and/or dispersing nano-object.

The paper is organized as follows. Section 2 describes the experimental method. Section 3 provides a model description of the setup based on Jones algebra. In section 4 we discuss a few experiments that were performed with the setup. In particular, we characterize the setup by comparing data to the mathematical model (subsection 4.1), we perform a noise analysis showing that our setup is detection-limited but very close to the photon-noise limit (subsection 4.2), and we provide some examples of measurements on single gold nanoparticles (subsection 4.3).

2. Experimental Method

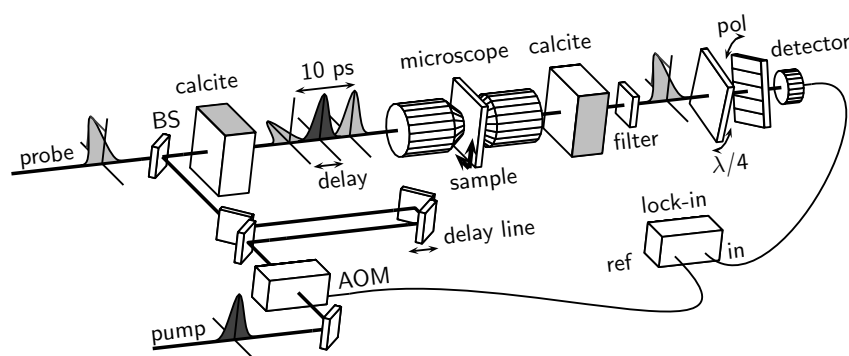


Fig. 1. Schematic drawing of the pump-probe common-path interferometer. A pump pulse and a pair of reference and probe pulses are focused on the sample in a microscope. The reference-probe pulses arise from a single pulse, split in time (10 ps delay) and polarization by a properly oriented birefringent calcite crystal. The delay between the pump pulse and the reference-probe pair can be scanned with a delay line. After the microscope, probe and reference are recombined by a second crystal and their interference monitors pump-induced changes in the optical properties of the sample. A quarter-wave plate ($\lambda/4$) and a polarizer (pol) are independently rotated to set the working point of the interferometer. The other details are described in the text.

We have designed a polarization-based common-path interferometer that uses two birefringent crystals to split and recombine the probe and reference waves [5]. A sketch of the setup is shown in Fig. 1. A laser pulse that is initially polarized at 45 degrees from vertical is split into two orthogonal polarization directions by the first calcite crystal, whose fast optical axis is vertical. Propagation in the thick (15 mm) birefringent crystal delays one of the polarizations by a time longer than the pulse length. This effectively creates two pulses, a probe and a reference, which are orthogonally polarized and have a mutual delay of 10 ps. These pulses interact with the sample (a glass coverslide on which nanoparticles are spincoated) in the microscope.

Behind the microscope, probe and reference are recombined by a second crystal, identical to the first one but oriented perpendicularly, its fast axis now being horizontal. With an analyzer assembly of a quarter-wave plate and a polarizer, the recombined waves are projected onto the same polarization state and interfere. Independently rotating the quarter-wave plate and the polarizer allows us to tune the relative contributions of the phase and amplitude of the probe

and reference waves. The interference reports on changes of the sample over the time interval between the probe and the reference pulses. In order to generate and accumulate the signal, we induce a change of the sample by means of a separate laser pulse, in a pump-probe configuration. This pump pulse (from a synchronous second laser source) is intensity-modulated by an acoustic-optical modulator (AOM) and travels over a variable delay line, before it is overlapped by a dichroic beam splitter (BS) with the probe beam. Dichroic filters efficiently prevent pump light from reaching the detector. By varying the delay between the pump pulse and the pair of probe and reference pulses, we can measure the ultrafast dynamics of our sample.

Let us schematically describe the working of the ideal interferometer with proper settings of the analyzer assembly. If the sample does neither modify the phase nor the amplitude of the probe with respect to those of the reference (e.g., if the pump laser is switched off, or if there is no particle in the laser focus), the polarization state after recombination is again linear, rotated by 45 degrees from the vertical. If we now switch on the pump laser while a nanoparticle sits in the common focus of the two laser beams, a small change in the phase and/or amplitude of the probe pulse will modify the polarization state after recombination, giving rise to a slightly elliptical and/or rotated linear polarization. This changes the transmission through the analyzer assembly. The change in polarization state is thus translated into a change of intensity at the detector, which we can measure with a lock-in amplifier synchronized with the pump's modulation.

With the quarter-wave plate and the polarizer, we can tune the fraction of the light that reaches the detector. If the quarter-wave plate has one of its optical axes parallel to the polarization direction of the incoming light, and if the polarizer is perpendicular to the incoming polarization, the detected intensity is minimized, and the interferometer is in a dark fringe. By rotating the polarizer by 90 degrees, we find a bright fringe, where the detected intensity has a maximum. Besides tuning the fraction of probe light that reaches the detector, we can also use the quarter-wave plate and the polarizer to select a working point where either phase or amplitude modifications of the probe field by the sample can be detected, independently from each other. If quarter-wave plate and polarizer are rotated in such a way that the amplitudes of the interfering fields are equal, but the phases are different, the interference term will only report on phase changes of the probe – assuming small changes to the fields as it is the case with nanoparticles. Conversely, if the polarizer and the quarter-wave plate are tuned so that the amplitudes are different while the phases are the same, the interferometer only senses amplitude changes of the probe, while phase changes remain unnoticed. The precise orientations of the polarizer and the quarter-wave plate for which the interferometer is either purely amplitude-sensitive or purely phase-sensitive are calculated in section 3 using a model based on Jones matrices.

Key features of our interferometer are the birefringent crystals for temporal beam splitting and recombination. Although they have the disadvantage that the delay between the probe and the reference pulse is fixed, the alignment becomes much easier, since it is not necessary to align the overlap of the spatial paths of the two interferometer arms. This considerably improves the visibility of the interferometric fringes. The crystals are 15-mm thick calcite crystals, cut from the same slab to make them as alike as possible. In order to keep the operation of the interferometer stable, we had to actively stabilize the temperature difference between the two crystals. No special temperature or mechanical stabilization is needed for the other elements in the beam path as they affect probe and reference in exactly the same manner.

If there is a small difference between the optical path lengths through the crystals, either because of a difference in orientation, temperature, or because of a difference in thickness (the crystals are specified to be equally thick to within 1 μm), we will have to allow for a static change in the polarization state of the probe beam after recombination. Instead of being linear at 45 degrees, the recombined beam can be elliptically polarized with a rotated axis, even when

the pump is off. A second static effect that must be taken into account is a residual difference in the transmissions of the vertical and horizontal polarizations by the microscope. These two effects change the orientations of the quarter-wave plate and the polarizer at the dark fringe, and the settings of the phase-sensitive and amplitude-sensitive working points. These experimental imperfections, however, can be included into the model of section 3. By measuring them, we can determine and compensate for their influence on the response of the interferometer. The quality of an interferometer can be characterized by its contrast ratio I_{max}/I_{min} . It can be shown that the previous effects, if properly compensated for, do not reduce the contrast. The contrast ratio is in fact limited by other imperfections of the optical elements, such as depolarization by the microscope objectives.

To generate our probe beam, we start with the signal beam of an OPO (APE, Berlin) synchronously pumped by a Ti:Sapphire laser (Coherent Mira 900D) at a repetition rate of 76 MHz. The signal beam is frequency-doubled in the OPO cavity. The resulting pulses are nearly Fourier-limited and are tunable in wavelength between 520 and 650 nm. The Ti:Sapphire laser is operated at 800 nm, and pumped by a CW frequency-doubled Nd:YAG laser (Coherent Verdi V10, 10 W, 532 nm). The laser system can be aligned to produce pulse lengths either in the picosecond or in the femtosecond range. The pulse lengths (full width at half maximum of the autocorrelation function) of the Ti:Sapphire laser and the OPO are approximately 3 ps and 1.5 ps in the picosecond configuration and 120 fs and 250 fs in the femtosecond configuration. Unless otherwise indicated, the measurements in this article were carried out in the femtosecond configuration.

A small part of the Ti:Sapphire laser beam, split off before entering the OPO, serves as the pump in the experiment. The pump beam travels over a variable delay stage to tune its time of arrival with respect to that of the probe-reference pair (see Fig. 1). The pump beam is combined with the probe beam by a dichroic beam splitter before the first crystal. The pump polarization is kept parallel to one of the optical axes of the crystal, to ensure that this pulse is not split. After the objectives, the residual pump light is filtered out by optical bandpass filters.

The home-built microscope consists of two objectives, an oil-immersion objective (NA 1.4) for excitation and an air-spaced objective (NA 0.95) for collection. The sample is mounted on a piezo-electric stage and can be scanned with 25-nm precision. Commercial gold nanoparticles (purchased from British Biocell International and Sigma-Aldrich and used without further treatment) were dispersed in a 10 mg/ml aqueous solution of polyvinyl alcohol and the resulting suspension was spin-coated onto a clean glass microscope cover slide.

Our detector is an analog Silicon APD (Hamamatsu C5331-11), which is sensitive for signals modulated at frequencies between 4 kHz and 100 MHz. The smallest optical signal that can be detected against electronic noise, called the noise-equivalent power (NEP), is specified between 0.5 and 1 pW/ $\sqrt{\text{Hz}}$. The detector signal is fed into a lock-in amplifier (Stanford SR844), whose internal clock drives an acousto-optical modulator (AOM) in the pump path at 400 kHz. To prevent overload of the lock-in from the 76 MHz signal of the laser pulses, the signal from the detector is pre-filtered with a passive 12 MHz low-pass filter.

Note that although we only describe a transmission configuration for the interferometer in this paper, it is in principle also possible to apply our method to reflection measurements. In that case, only one calcite crystal is necessary, but a quarter-wave plate has to be introduced between the crystal and the microscope to ensure that the pulses are recombined when travelling through the crystal in the backward direction.

3. Model of the interferometer

We model our interferometer by representing each element by a Jones matrix. In this way, we obtain analytical expressions for the intensity at the detector and for the measured signal, as

functions of the angles of the quarter-wave plate ϕ and of the polarizer θ (see Fig. 1). We calculate the contribution to our signal of real and imaginary changes in the electric field of the probe for each θ and ϕ and calculate for which combination of angles we can measure the real and imaginary changes separately.

From Fig. 1, we write all elements of the interferometer as Jones matrices. Matrix multiplication of the elements with the incoming probe field will yield the electric field and subsequently the intensity at the detector.

The input wave is polarized at -45 degrees, $E_{in} = \sqrt{1/2}(1, -1)$, and is split into a horizontally polarized reference wave, which travels in front, and a vertically polarized probe. The absorption of the pump pulse by the particle triggers a small time-varying modification $\zeta(t)$ in the fields transmitted through the microscope. The modification ζ is complex-valued, allowing for changes in amplitude and phase of the fields. The temporal zero is the arrival of the pump pulse at the sample. Reference and probe pulses are orthogonally polarized on each other and delayed by 10 ps. After recombination, the Jones matrix associated with the particle can be written as

$$\mathbf{P} = \begin{pmatrix} 1 + \zeta_H(t - 10\text{ps}) & 0 \\ 0 & 1 + \zeta'_V(t) \end{pmatrix}. \quad (1)$$

Shape and orientation of the particle are *a priori* unknown, and a difference in particle response in the horizontal and vertical direction has to be taken into account, and is here indicated with the indices H and V . Also, the field of the reference pulse might alter the state of the particle, which changes the particle response to the probe pulse from $\zeta(t)$ to $\zeta'(t)$. Including these two effects would however lead to more parameters than are solvable, so we assume for now that the particle is symmetric for the horizontal and vertical direction (so either spherical, or spheroid with the two equal axes in the x-y plane), and that we are in a linear-response regime, where the state of the particle is not affected by the field of the reference pulse. We can now write, instead of Eq. (1),

$$\mathbf{P} = \begin{pmatrix} 1 + \zeta(t - 10\text{ps}) & 0 \\ 0 & 1 + \zeta(t) \end{pmatrix} \approx \begin{pmatrix} 1 & 0 \\ 0 & 1 + \Delta\zeta(t) \end{pmatrix}, \quad (2)$$

where $\Delta\zeta(t) = \zeta(t) - \zeta(t - 10\text{ps})$ is the 10-ps difference in the pump-induced modification of the field. The approximation is exact for $t < 10\text{ps}$ as then $\zeta(t - 10\text{ps}) = 0$, and introduces only small errors for working points of the interferometer close to the dark fringe for all other delays t .

As was already mentioned in section 2, it is important to consider a difference in optical path length through both crystals and a difference in transmission of probe and reference through the microscope. The former effect manifests itself as an additional wave plate in the optical path, while the latter can be modelled with a relative decrease in amplitude of one of the two arms. In the model, we can combine both effects in one matrix \mathbf{D} , which adds two additional parameters, ρ for the difference in transmission between the two polarizations (dichroism), and τ for the optical-path difference:

$$\mathbf{D}(\rho, \tau) = \frac{1}{1 + (1 - \rho)^2} \begin{pmatrix} 1 & 0 \\ 0 & (1 - \rho) e^{i\tau} \end{pmatrix}. \quad (3)$$

The prefactor is introduced for normalization of the bright fringe intensity. ρ and τ can be determined experimentally, since a change in either of them causes the dark fringe of the interferometer to deviate from its original position $(\theta, \phi) = (45^\circ, 45^\circ)$. Therefore, by measuring the actual position of the dark fringe, the two calibration parameters ρ and τ can be calculated.

The Jones matrices of a quarter-wave plate \mathbf{Q} and of a polarizer \mathbf{L} oriented at an arbitrary angle are found by multiplying the Jones matrices for the elements at 0 degree [24] by rotation

matrices:

$$\mathbf{Q}(\phi) = \frac{1}{\sqrt{2}} \begin{pmatrix} 1 + i\cos(2\phi) & i\sin(2\phi) \\ i\sin(2\phi) & 1 - i\cos(2\phi) \end{pmatrix}, \quad (4)$$

$$\mathbf{L}(\theta) = \frac{1}{2} \begin{pmatrix} 1 + \cos(2\theta) & \sin(2\theta) \\ \sin(2\theta) & 1 - \cos(2\theta) \end{pmatrix}. \quad (5)$$

The combined action of the elements in Eqs. (2) to (5) on the incoming wave E_{in} now gives the electric field and the intensity of the probe beam at the detector:

$$\mathbf{E}_{det}(\theta, \phi, \rho, \tau, \Delta\zeta) = \mathbf{L}(\theta) \cdot \mathbf{Q}(\phi) \cdot \mathbf{D}(\rho, \tau) \cdot \mathbf{P}(\Delta\zeta) \cdot \mathbf{E}_{in}, \quad (6)$$

$$I_{det}(\theta, \phi, \rho, \tau, \Delta\zeta) = |\mathbf{E}_{det}(\theta, \phi, \rho, \tau, \Delta\zeta)|^2. \quad (7)$$

A contour plot of the detected intensity I_{det} as a function of θ and ϕ with $\rho = 0$, $\tau = 0$ and $\Delta\zeta = 0$ is given in Fig. 2. The intensity has a minimum (dark fringe) for $(\theta, \phi) = (45^\circ, 45^\circ)$, increases outwards in an elliptical shape, and at $(\theta, \phi) = (45^\circ, 135^\circ)$ we find a bright fringe.

Essentially, with a lock-in amplifier, we subtract the detected intensity of the probe beam when the pump is off from the detected intensity when the pump is on, which gives a signal of

$$S(\theta, \phi, \rho, \tau, \Delta\zeta) = I_{det}(\theta, \phi, \rho, \tau, \Delta\zeta) - I_{det}(\theta, \phi, \rho, \tau, 0). \quad (8)$$

In general, for a given value of θ and ϕ , there will be both a contribution from the real and imaginary part of $\Delta\zeta$ to the signal in Eq. (8), corresponding to amplitude and phase changes of the field, respectively. They cannot be detected separately, except for configurations where either the amplitude contribution or the phase contribution is zero. For these working points, the detected signal will consist of either the pure phase contribution, or the pure amplitude contribution. In the following we call amplitude working point a configuration of the interferometer which is *not* sensitive to a phase change in the field. All these amplitude working points form a line which we will call amplitude line. It is the zero contour of the response to a phase change, i.e. imaginary $\Delta\zeta$ in Eq. (8). In the same way, a phase working point is a configuration of the interferometer which is not sensitive to an amplitude change of the field. The amplitude and phase lines are shown in Fig. 2.

Our model is fully analytical, and is in principle exact for a weak enough probe pulse. It gives the measured signal in terms of θ , ϕ , ρ , τ , and $\Delta\zeta$, but this expression is too lengthy for a qualitative discussion. Instead, we will give a first-order expansion in θ and ϕ around the dark fringe, which provides an illustrative explanation of the working of the interferometer and of the separation of phase and amplitude.

From Fig. 2(A) we see that the interferometer is in the dark fringe if the quarter-wave plate's fast axis and the polarizer's transmission axis are both oriented at +45 degrees. For a first order approximation, we only consider small deviations from the dark fringe: $\hat{\theta} = \theta - \frac{\pi}{4}$ and $\hat{\phi} = \phi - \frac{\pi}{4}$. Using the small-angle approximation, neglecting all higher-order terms of $\hat{\theta}$ and $\hat{\phi}$, and disregarding the experimental correction parameters ρ and τ , we find the total intensity at the detector

$$I_{det} = |\mathbf{E}_{det}|^2 = \left(\hat{\theta} - \hat{\phi} - \frac{\text{Im}(\Delta\zeta)}{2} \right)^2 + \left(\hat{\phi} + \frac{\text{Re}(\Delta\zeta)}{2} \right)^2, \quad (9)$$

while the intensity at the detector without the pump ($\Delta\zeta = 0$) is

$$I_0 = (\hat{\theta} - \hat{\phi})^2 + \hat{\phi}^2. \quad (10)$$

We thus find our signal, which is the first-order change in intensity

$$S = I_{det} - I_0 = \hat{\phi} \text{Re}(\Delta\zeta) - (\hat{\theta} - \hat{\phi}) \text{Im}(\Delta\zeta). \quad (11)$$

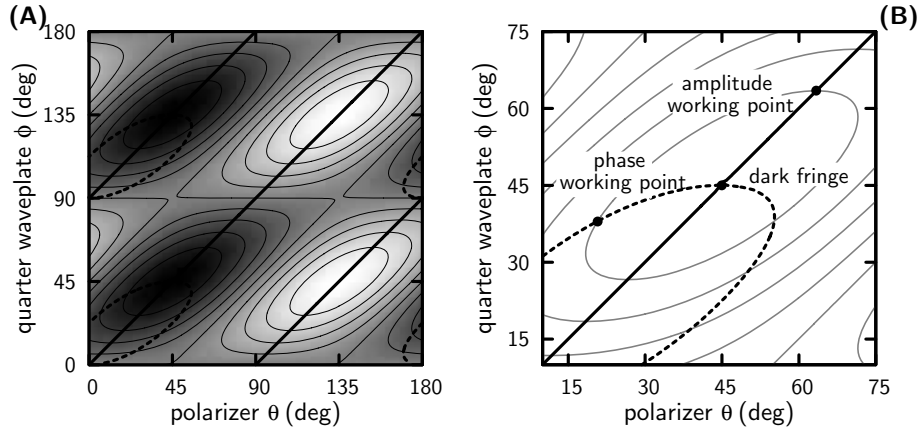


Fig. 2. (A) Contour plot of the intensity at the detector as a function of the angle of the quarter-wave plate and the polarizer, showing bright and dark fringes. On the thick lines, the interferometer is sensitive to either amplitude changes only (solid) or phase changes only (dashed). (B) Magnification around a dark fringe, additionally showing two working points of the interferometer where to detect pure amplitude or phase signals.

From Eq. (11) it is easy to see that amplitude and phase responses can be separated by choosing proper angles for the polarizer and the quarter-wave plate. If $\hat{\theta}$ and $\hat{\phi}$ are equal and nonzero, the interferometer is sensitive for amplitude changes only, while if $\hat{\phi} = 0$ and $\hat{\theta} \neq 0$, the interferometer only measures phase changes. Fig. 2(B) shows that this first-order approximation still applies for the amplitude line even for large angles, while the phase line is described by $\hat{\phi} = 0$ only very close to the dark fringe.

4. Results and discussion

4.1. Characterization of the interferometer

The contrast ratio of the interferometer (I_{max}/I_{min}), found by rotating the polarizer by 360 degrees as shown in Fig. 3(A), reaches 150 in the case shown here and varies typically between 100 and 200. This corresponds to a fringe visibility (defined as $(I_{max} - I_{min})/(I_{max} + I_{min})$) between 98% and 99%. The contrast is mainly limited by depolarization by the microscope objectives and by the quality of the crystal surfaces. Nevertheless, due to the simplified alignment of the crystals, the fringe visibility is high compared with other implementations of interferometric microscopes (90% ref. [23], 66% ref. [18]). As expected, the model describes the position of the equal-intensity contours, as shown in Fig. 3(B) for the 10% contour line.

The detection path was calibrated by a laser beam square-modulated at the lock-in reference frequency. In the following we give, if not otherwise mentioned, the root-mean-squared (rms) values of the pump-induced square modulation to our probe beam. To be independent of the absolute probe power, we normalize the detected intensity modulation ΔI to the intensity of the bright fringe I_{bright} . For a constant relative change in the probe field $\Delta\zeta$, the measured and calculated intensity changes ΔI depend on the working point as plotted in Fig. 3(C) and (D). In order to calibrate $\Delta\zeta$, we notice that at half-fringe on the amplitude line the reference is fully blocked, and $\Delta\zeta = \Delta I/I_{bright}$.

Fig. 3(C) and (D) compare the detected intensity modulation as a function of the interferometer fringe level for working points on the amplitude (Fig. 3(C)) and phase line (Fig. 3(D)).

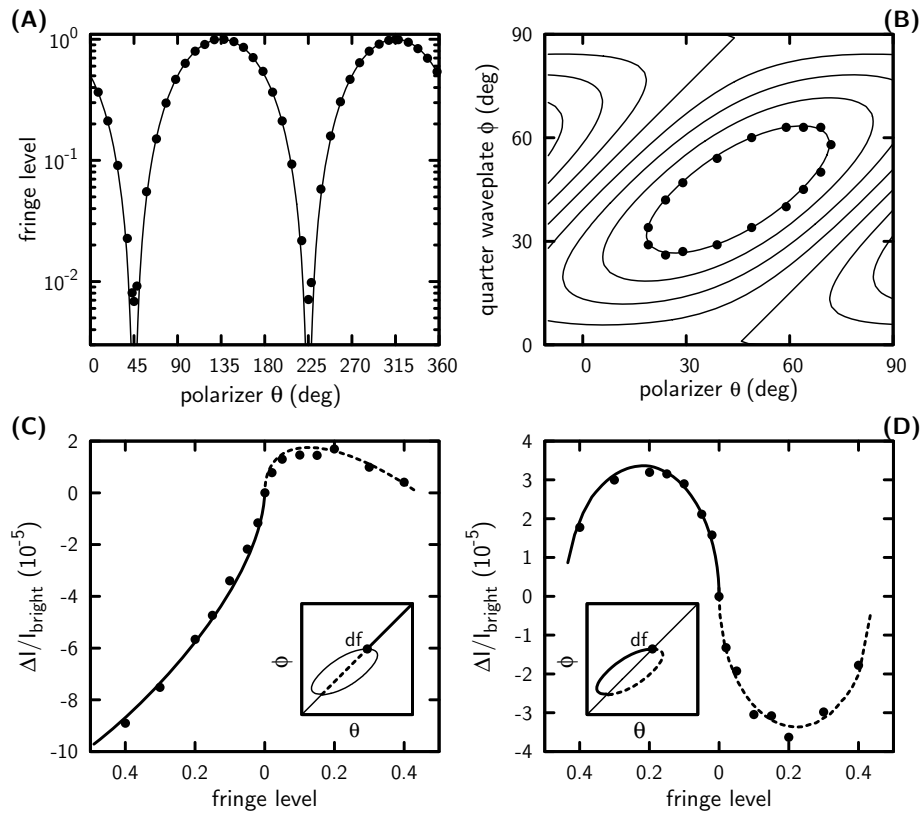


Fig. 3. (A) The contrast ratio of the interferometer amounts to 150 as measured by scanning the polarizer angle (dots). The model (line) assumes infinite contrast, i.e. an absolute zero at the dark fringe. (B) The position of the 10%-fringe level is well described by our model (intensity contour lines in steps of 0.1). (C, D) Signal from a single 60-nm gold nanoparticle, measured along the amplitude working line (C) and along the phase working line (D). The lines are the signals as calculated by the model assuming $\Delta\zeta = (-9.3 + 10.2i) 10^{-5}$. The insets depict the corresponding positions of the polarizer (θ) and the quarter-wave plate (ϕ) relative to the dark fringe (df). The measurement in panel (B) was carried out in the picosecond configuration.

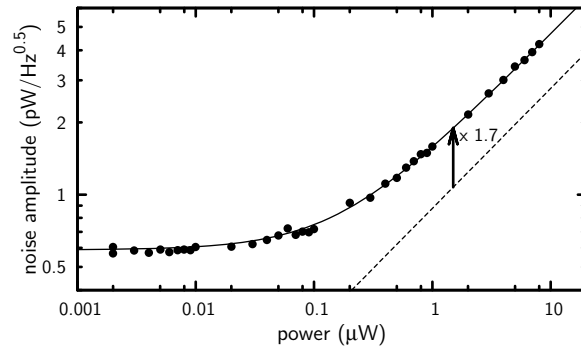


Fig. 4. Noise amplitude as a function of the optical power at the detector. The solid line is a fit to Eq. (13), with $\sigma_{amp} = 0.6 \text{ pW}/\sqrt{\text{Hz}}$, $n_{laser} = 0$, and $F = 3 \approx 1.7^2$. The dashed line describes the expected photon noise scaling as the square-root of the probe power. The difference is due to the excess noise of the avalanche process in the analog detector. This experiment was carried out in the picosecond configuration.

The probe modulation was caused by a single 60-nm gold particle in the focus under constant pump. The data is well described by our model with a pump-induced field modification of $\Delta\zeta = (-9.3 + 10.2i) 10^{-5}$ as the only free parameter.

Note that the exact definition of $\Delta\zeta$ used in this article differs from that used in our previous publication [5]: we now give rms instead of peak-peak values to facilitate comparison with noise levels and the change in the probe field is given relative to the field at the sample and not to the field at the detector. Both corrections reduce the absolute value of $\Delta\zeta$ by a factor of $2\sqrt{2} I_{\text{bright}}/I_{\text{wp}}$. The ratio $I_{\text{wp}}/I_{\text{bright}}$ used in Ref. [5] was given in the supplementary material. In the linear-response regime it is possible to calculate the pump-induced change of the probe field $\zeta(t)$ from $\Delta\zeta(t)$ (Eq. 2). However, this assumption is too crude for our experimental conditions, and the full nonlinear response must be calculated for a quantitative agreement between predicted and measured $\zeta(t)$ traces. This calculation is however beyond the scope of this paper.

4.2. Noise

In an optical experiment, we have to consider two independent sources of noise, electronic noise and optical shot noise, which add quadratically. Optical noise itself has two causes. On the one hand, laser noise σ_{laser} stems from classical fluctuations in the output power of the laser, and usually grows linearly with laser power. The photon noise σ_{ph} , on the other hand, originates from quantum-mechanical uncertainty in the amplitude of the electric field of the laser wave and grows as the square root of laser power. Unless squeezed light is used, photon noise is the fundamental noise limit. Photon noise is given by [25]

$$\sigma_{ph} = \sqrt{2BP h\nu} \quad , \quad (12)$$

where B is the detection bandwidth and P is the detected optical power.

The electronic noise also has two dominant sources. One is the thermal noise of the amplification stage of the detector (σ_{amp} , dark noise), which is specified by the noise equivalent power (NEP), and is independent of laser power. Another source of electronic noise, the excess noise, is specific for the analog avalanche photodiodes used here [26]. It arises from statistical fluctuations in the avalanche process following the absorption of every photon. Because it is

related to the detection of photons, excess noise has the same statistical properties as photon noise and also increases as the square root of laser power. The excess noise factor F is defined as $\sigma_{shot}^2 = F \sigma_{ph}^2$, where σ_{shot} is the full shot noise. The total noise amplitude σ_{tot} then amounts to

$$\sigma_{tot} = \sqrt{\sigma_{ampl}^2 + \sigma_{shot}^2 + \sigma_{laser}^2} = \sqrt{\sigma_{ampl}^2 + F 2 B P h \nu + (n_{laser} P)^2} \quad (13)$$

The noise is measured as the standard deviation of a series of calibrated root-mean-square values given by the lock-in amplifier. This is equivalent to the standard deviation of a series of absolute power measurements in the given bandwidth B . Fig. 4 shows the measured noise as a function of the probe power at the detector (note that, as long as the pump laser is sufficiently rejected from the detector with dichroic filters, there is no pump-power dependence of the noise level). At low power, the electronic noise dominates and we find a constant contribution of $0.6 \text{ pW}/\sqrt{\text{Hz}}$, within the specification of the NEP of the detector (section 2). At higher power, the optical noise becomes dominant and in this regime, the noise scales as the square-root of the laser power. The power range in Fig. 4 was limited by saturation of the detector. Within this range, there is no contribution that scales linearly with laser power, which means that laser noise does not contribute to the total noise. For detected powers levels between 1 and $10 \mu\text{W}$, the main noise component is shot noise. The expected photon noise as a function of laser power is indicated with a dashed line in Fig. 4. The difference arises from the excess noise generated by the avalanche photodiode and is described by an excess noise factor $F = 3 \approx 1.7^2$, in good agreement with the manufacturer's specification. Replacing the avalanche diode by a PIN diode will remove this excess-noise contribution, if a sufficiently low-noise amplifier is used. The analysis of noise sources in our experiment shows that the interferometer is not absolutely required to reduce noise from fluctuations of the light sources (laser noise), as our laser and OPO systems are very stable. A much simpler experimental setup in a pump-probe configuration would therefore suffice to provide information on transient absorption only (i.e., on the amplitude signal).

4.3. Gold nanoparticles

As an illustration of some of the possibilities of our method, we show experiments on single gold nanoparticles. More exhaustive results have been published elsewhere [5]. In metal nanoparticles, optical contrast is mainly provided by the surface plasmon-polariton, or Mie resonance [27]. The Mie resonance is a collective oscillation of the free electrons in the particle, and manifests itself as a relatively broad nearly-Lorentzian peak in the absorption spectrum. The position and width of the peak depend on the size and shape of the particle, and on its environment [27]. If a particle is excited by a short near-infrared laser pulse, first only free electrons are excited. By electron-electron scattering, a thermalized electron gas is quickly formed, which leads to a short but strong increase in the electron pressure [28] and a broadening of the plasmon resonance [29]. The electrons subsequently cool by electron-phonon coupling on a timescale of about 1 ps, hereby heating the lattice. Note that this cooling time depends on the intensity of the excitation [30]. This sudden heating of the lattice, together with the short peak of electronic Fermi pressure immediately after absorption of the light pulse, launches an acoustic vibration in the lattice [28], which manifests itself optically as a periodic red shift of the plasmon resonance [30, 31]. The period of this radial breathing mode is given in Lamb's theory [32] as a function of the particle size and of the longitudinal and transverse sound velocities of the metal [33]. The period is on the order of 20 picoseconds for free gold spheres of about 60 nm diameter. On a longer timescale (100-1000 ps), the lattice cools through heat conduction to the environment.

In Fig. 5(A), a confocal scan of a sample containing 10-nm gold nanoparticles is shown. Each diffraction-limited spot is caused by a single nanoparticle [5]. The background consists only of

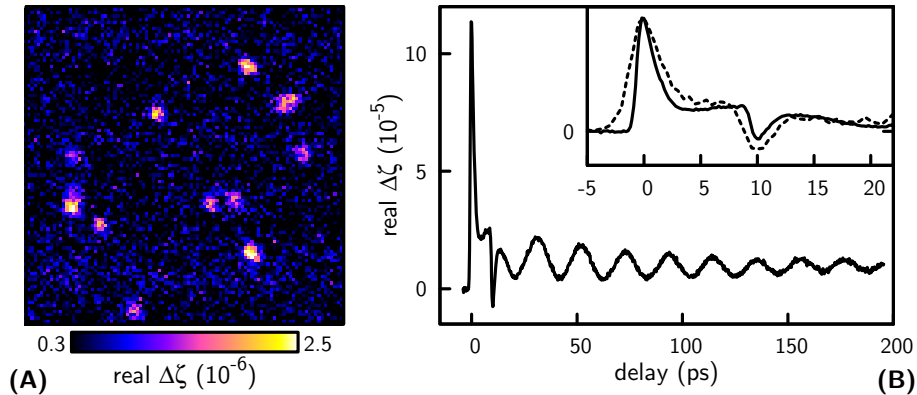


Fig. 5. (A) Confocal scan of a $10 \mu\text{m} \times 10 \mu\text{m}$ area of a sample containing 10-nm gold nanoparticles. Each diffraction limited spot is caused by a single nanoparticle. The background contains only the noise discussed in section 4.2. Probe wavelength and pump-probe delay were optimized for maximum contrast (532 nm, 0 ps, respectively). This experiment was carried out in the picosecond configuration. The sampling time was 200 ms per pixel. (B) Example of a delay scan of a single 60-nm gold nanoparticle showing a short spike due to the hot electron gas and periodic oscillations of the particle size. The inset compare the 'femtosecond' (solid) and the 'picosecond' (dashed) configuration of the laser system in their resolving power of the fast electronic process. The traces in the inset are normalized to the first peak. The detection bandwidth was 7.8 Hz.

the noise discussed in section 4.2. The delay between the pump and the probe-reference pair was tuned such that the pump and the probe arrive at the sample simultaneously. In this way, we measure the prompt response of the nanoparticle to the excitation, which gives the highest contrast on the real part of the signal (absorptive response). The wavelength of the probe was tuned to the plasmon resonance of the particles at 532 nm, again to ensure maximum contrast. With a sampling time of 200 ms per pixel, the particles are detected with a signal-to-noise ratio of roughly 7. Pump and probe power are limited by the maximum permissible absorption in the particle, which results in a detection limit of 10-nm diameter for gold nanoparticles, for reasonable sampling times shorter than one second per pixel.

We measure the time-dependent response of the nanoparticle to excitation with the pump pulse by varying the delay between the pump pulse and the probe-reference pair of pulses. Fig. 5(B) shows an example of the response of a single 60-nm gold nanoparticle in the laser focus, detected with a bandwidth of 7.8 Hz. The first part of the trace, which is enlarged in the inset, shows two sharp peaks, that occur when the pump is overlapped with the probe and with the reference respectively. These peaks stem from the change in optical response due to the hot electron gas. From the rise and decay times of the peaks, the electron-electron scattering and electron-phonon coupling times can be obtained [30, 34]. Since these processes take place on timescales faster than a picosecond, the width of the peaks is dominated by the pulse length if the measurement is carried out with picosecond pulses, and information on the electronic decay times of the particle is lost. However, by using shorter pulses, it is possible to resolve these processes. This is demonstrated in the inset of Fig. 5(B), where the fast electronic response is measured with femtosecond and picosecond pulses on two different single particles. In the femtosecond experiment, the peaks are narrow enough to resolve the electronic processes in the particle. On a longer timescale, the signal shows a damped harmonic oscillation. This is a direct

observation of the acoustic vibrations of the particle, from which we can derive information on the elastic properties of the particle itself and its mechanical coupling to the surroundings.

In Fig. 6, we combine the amplitude and phase separation with time-resolved experiments, in order to measure the complete complex temporal response of the particle. As mentioned in section 3, for delay times larger than 10 ps, it is important to choose a working point close to the dark fringe, to ensure the full separation of amplitude and phase. The interferometer was tuned to a 2% fringe, to comply with the approximation of Eq. (2). In Fig. 6(A), the real and imaginary temporal responses of a single particle are shown together. Here, the different spectral origin (resonance broadening versus red shift) of the peaks and of the oscillations becomes apparent, since the two peaks have the same sign in both the amplitude and the phase configuration, while the vibrations are exactly out of phase. Figure 6(B) shows the real and imaginary temporal response of another particle in the same sample. While the amplitude response of this particle is nearly the same as that of the particle in Fig 6(A), the phase response is rather different. The electronic contribution gives a mainly dispersive response, while the acoustic vibrations are completely absorptive. The differences between the two particles can be visualized in a different manner in Fig. 6(C), where the dispersive response is plotted against the absorptive response for both particles. The trace of the particle from Fig. 6(A) (gray) shows a weaker electronic response, while the overall trace is tilted towards the real axis. These kind of differences between particles can arise from differences in their spectral responses, themselves due to differences in their size, shape or local environment. Further study is needed to precisely correlate the optical and structural properties of the particles, but there is little doubt that single-particle studies of gold nanoparticles will lead to a better understanding of their properties, and to such applications as elasticity and damping sensors at nanometer scales.

5. Conclusion

We have developed a common-path interferometer, which enables time-resolved experiments on single nanoparticles, and with which the absorptive and dispersive responses of the particles can be separated. The design of the interferometer, using birefringent crystals as splitting elements, simplifies the alignment and increases the fringe contrast. A noise analysis showed that the detection is shot-noise limited, just a factor of about 1.7 above the ultimate limit of photon noise. We expect to reach the photon-noise limit by replacing the avalanche diode with a good PIN diode. The interferometer is fully described by an analytical model, which allows us to find optimal working points. We have successfully used our method for time-resolved experiments on single gold nanoparticles. While also direct absorption measurements on single particles yield the ultrafast response of the hot electron gas [8], only an interferometric experiment provides the full complex response of a nanoparticle on the sub-picosecond timescale, free from any model or assumption.

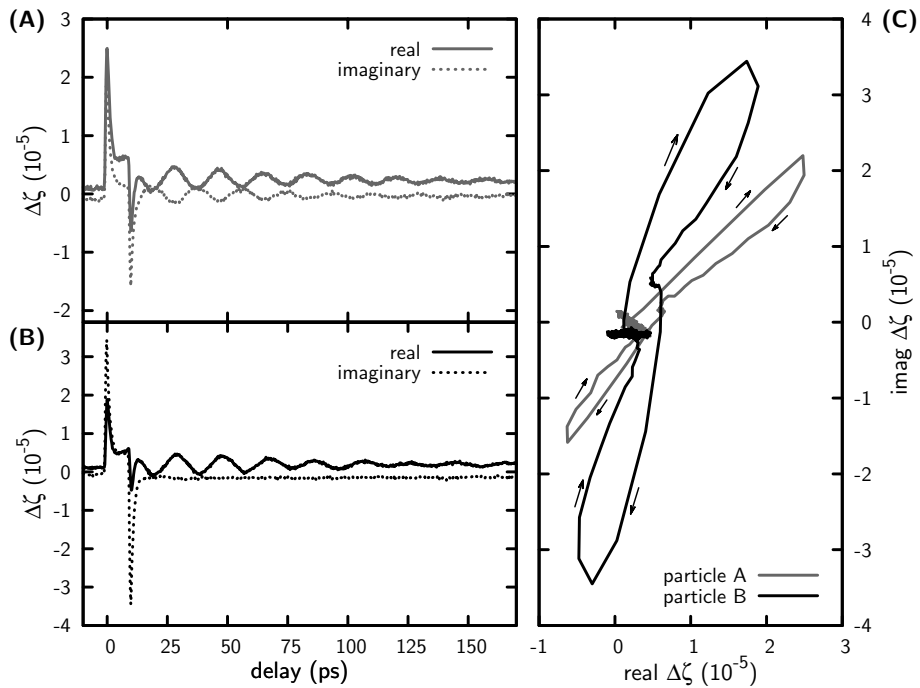


Fig. 6. (A,B) Delay scans of two gold nanoparticles with a nominal diameter of 60 nm, measured at the amplitude (solid) and phase (dotted) sensitive working point. For particle (A), the peaks have the same sign, but the sign of the vibrations is opposite demonstrating the different spectral origin. For the particle in panel (B), the dispersive contribution to the peaks is much stronger, while the vibrations completely vanish in this phase-sensitive configuration. (C) Plotting $\text{Im}(\Delta\zeta)$ against $\text{Re}(\Delta\zeta)$ reveals the full response of both particles in the complex plane. The arrows indicate the time evolution. In all plots, the detected intensity was 2% of the bright-fringe intensity. The traces show the average of five measurements, each with a detection bandwidth of 7.8 Hz.